Efficient finite-difference time-domain computation of resonant frequencies of rectangular Lamé mode resonators via a combination of the symmetry boundary conditions and the Padé approximation

Takashi Yasui*[,1], Koji Hasegawa[2], and Koichi Hirayama[1]

[1]*Kitami Institute of Technology, Kitami, Hokkaido 090-8507, Japan*
[2]*Muroran Institute of Technology, Muroran, Hokkaido 050-8585, Japan*

Resonant frequency analysis of the fundamental and higher-order modes of Lamé mode resonators on a lossless isotropic solid is carried out by the finite-difference time-domain (FD-TD) method with the staggered grid with collocated grid points of velocities (SGCV). The symmetry boundary condition is implemented to reduce the size of the computational domain for the FD-TD method with the SGCV. One spectrum estimation technique based on the Padé approximation is employed to effectively extract the resonant frequencies from a spectrum transformed from the time series data calculated by the FD-TD method. Numerical results show the validity and efficiency of these techniques.

1. Introduction

The finite-difference time-domain (FD-TD) method is a powerful and attractive tool for modeling the propagation and scattering of acoustic[1–8] or elastic[9–22] waves. Discretization of two first-order partial differential equations with finite-difference approximations results in a staggered grid (SG),[9,10] a rotated SG[11,12] a diagonal SG,[13–15] a Lebedev grid,[16–18] or an SG with collocated grid points of velocities (SGCV).[19–21]

The SGCV was proposed for FD-TD analysis of elastic-wave propagation in anisotropic solids.[19] Since the SGCV is derived from a single control volume of the momentum conservation law and line integration of the displacement gradient, boundary conditions are simply imposed on the FD-TD method.

To demonstrate the simply imposed boundary conditions on free-surfaces, an FD-TD model with SGCV was applied to resonance frequency analysis of a Lamé mode resonator on a lossless isotropic solid, which has free-surfaces between the vacuum and the solid; the results showed good agreement with the analytical values.[20] It was also shown that the accuracies of results computed by SGCVs and SGs were comparable.[21]

*E-mail: yasui@mail.kitami-it.ac.jp

For resonant mode analysis, particle velocity and stress fields are either symmetric or antisymmetric with respect to axes of symmetry. It has been shown that imposing appropriate symmetry boundary conditions on axes of symmetry can effectively reduce the computational time for the resonant frequency analysis of the fundamental Lamé mode.[22)]

In addition, after the FD-TD calculation, we need to transform the calculated time response of the elastic field components into the frequency spectrum by FFT to extract resonant frequencies.[22)] However, an inherent limitation of the FFT approach is the inadequate frequency resolution. Thus, it is necessary to run the FD-TD calculation for a sufficiently large number of time steps. To overcome this limitation, Dey and Mittra apply one of the techniques for spectrum estimation, the so-called FFT/Padé technique,[23,24)] to electromagnetic wave cavity problems.

In this study, resonant frequency analysis by the FD-TD method with SGCV is carried out for the fundamental and higher-order modes of Lamé mode resonators on an isotropic solid. The symmetry boundary condition is implemented to reduce the size of the computational domain for the FD-TD method with the SGCV. The FFT/Padé technique[23,24)] is employed for efficient extraction of resonant frequencies from a spectrum transformed from a time response calculated by the FD-TD method. Numerical results show the validity and efficiency of these techniques.

2. Fundamental equations

Newton's equation of motion and Hook's law are respectively represented in a Cartesian coordinate system (x_1, x_2, x_3) as

$$\rho \frac{\partial v'_{x_k}}{\partial t} = \sum_{i=1}^{3} \frac{\partial T_{x_k x_i}}{\partial x_i} \ (k = 1, 2, 3), \tag{1}$$

$$\frac{\partial T_{x_i x_j}}{\partial t} = \sum_{k=1}^{3} \sum_{m=1}^{3} C'_{x_i x_j x_k x_m} \frac{\partial v'_{x_k}}{\partial x_m} \ (i, j = 1, 2, 3), \tag{2}$$

where t, ρ, v'_{x_i}, $T_{x_i x_j}$, and $C'_{x_i x_j x_k x_m}$ $(i, j, k, m = 1, 2, 3)$ are respectively the time, the mass density, the x_i-component of particle velocity, the $x_i x_j$-component of the stress tensor, and the $x_i x_j x_k x_m$-component of the stiffness tensor.

In this paper, we consider two-dimensional $[\partial/\partial x_3 = 0]$ rectangular Lamé mode resonators on an isotropic solid with the length L_2 and width L_1, as shown in Fig. 1. From Eqs. (1) and (2), we obtain the following normalized equations with abbreviated

subscripts:

$$\Delta_t \frac{\partial v_1}{\partial t} = R\Delta \left(\frac{\partial T_1}{\partial x_1} + \frac{\partial T_6}{\partial x_2} \right), \tag{3}$$

$$\Delta_t \frac{\partial v_2}{\partial t} = R\Delta \left(\frac{\partial T_6}{\partial x_1} + \frac{\partial T_2}{\partial x_2} \right), \tag{4}$$

$$\Delta_t \frac{\partial T_1}{\partial t} = R\Delta \left(C_{11} \frac{\partial v_1}{\partial x_1} + C_{12} \frac{\partial v_2}{\partial x_2} \right), \tag{5}$$

$$\Delta_t \frac{\partial T_2}{\partial t} = R\Delta \left(C_{21} \frac{\partial v_1}{\partial x_1} + C_{22} \frac{\partial v_2}{\partial x_2} \right), \tag{6}$$

$$\Delta_t \frac{\partial T_6}{\partial t} = R\Delta \left(C_{66} \frac{\partial v_1}{\partial x_2} + C_{66} \frac{\partial v_2}{\partial x_1} \right). \tag{7}$$

Here, $v_i = Z_0 v_i'$ $(i = 1, 2)$ and $C_{ij} = C_{ij}'/C_{11}'$ $(ij = 11, 12, 21, 22, 66)$ are respectively the normalized components of the particle velocity and stiffness tensor, where $Z_0 = \sqrt{\rho C_{11}'}$. We define the Courant number R as

$$R = \frac{V_p \Delta_t}{\Delta}, \tag{8}$$

where $V_p = \sqrt{C_{11}'/\rho}$, Δ, and Δ_t are respectively the phase velocity of the P-wave, the spatial interval of the grid, and the time interval.

3. Discretization and boundary conditions

For the FD-TD analysis, the computational domain is discretized with square SGCVs[20] with the side length Δ, as shown in Fig. 2. Here, I and J are integers for a grid point with the position vector $\boldsymbol{p} = (I\hat{x}_1 + J\hat{x}_2)\Delta$, where $\hat{x}_1$ and $\hat{x}_2$ are the unit vectors in the x_1- and x_2-directions, respectively. To discretize Eqs. (3) – (7), we use a scheme of second-order accuracy in the time and spatial differences. Bilinear interpolation with four adjoining grids is used to evaluate the gradients of particle velocity on grids just inside the free-surface boundaries at the edges of the resonators.[20,21]

At the edges of the resonators, the following free-surface boundary conditions are imposed:

$$T_1(x_1, x_2) = 0, \qquad T_6(x_1, x_2) = 0 \tag{9}$$

for $x_1 = \pm L_1/2$, and

$$T_2(x_1, x_2) = 0, \qquad T_6(x_1, x_2) = 0 \tag{10}$$

for $x_2 = \pm L_2/2$.

Owing to the symmetric distribution of elastic field components, required computational resources can be reduced by imposing the symmetry boundary conditions on the symmetry axes, $x_1 = 0$ and/or $x_2 = 0$, as shown in Fig. 3. In Fig. 3(a), the symmetry boundary condition is imposed on $x_2 = 0$, so that the size of the computational domain can be reduced to half of the domain. In Fig. 3(b), the symmetry boundary conditions are imposed on $x_1 = 0$ and $x_2 = 0$, so that the size of the computational domain can be reduced to one-quarter.

The parity of elastic field components on the symmetric boundaries is shown in Tables I and II. The particle velocity components, v_1 and v_2, located on the lines of $x_1 = -\Delta/2$ and $x_2 = -\Delta/2$ as shown in Fig. 3, are for a simple implementation of the symmetry boundary conditions. We copy the values of velocity components on $x_1 = \Delta/2$ and $x_2 = \Delta/2$ to those on $x_1 = -\Delta/2$ and $x_2 = -\Delta/2$, respectively, with consideration of the parity imposed on the condition. Note that the standard time-updating procedure[20] for the stress components automatically satisfies their symmetry conditions owing to the external particle velocity components.

4. Spectrum estimation with the Padé approximation

After an FD-TD calculation, we need to transform the calculated time response to the frequency domain using the FFT. An inherent limitation of this approach is the inadequate frequency resolution. Thus, it is necessary to run the FD-TD calculation for a sufficiently large number of time steps.

To overcome this limitation, Dey and Mittra[23,24] employ a two-step procedure, the so-called the FFT/Padé technique. First, the FFT is applied to the FDTD-calculated time response to obtain a frequency response. Then, the accuracy of the frequency response is improved with the Padé approximation.

Under the Padé approximation, the frequency response is represented as the ratio of two polynomials $Q_N(\omega)$ and $D_M(\omega)$ as follows:

$$P(\omega) \cong \frac{Q_N(\omega)}{D_M(\omega)}, \tag{11}$$

where

$$Q_N(\omega) = \sum_{i=0}^{N} \alpha_i \omega^i, \quad D_M(\omega) = \sum_{i=0}^{M} \beta_i \omega^i. \tag{12}$$

Here, α_i and β_i are unknown coefficients to be determined. We can rewrite Eq. (11) as

$$P(\omega_j) D_M(\omega_j) \cong Q_N(\omega_j), \tag{13}$$

where $P(\omega_j)$ denotes the value of the frequency response with the FFT at a sampling angular frequency ω_j ($j = 0, 1, \ldots, S-1$). Here, S is the number of sampling angular frequencies within the range of the FFT. We obtain a system of S equations for a total of $N + M + 2$ unknown coefficients, α_i ($i = 0, \ldots, N$) and β_i ($i = 0, \ldots, M$), as follows:

$$P(\omega_j)\sum_{i=1}^{M}\beta_i\omega_j^i - \sum_{i=0}^{N}\alpha_i\omega_j^i = -P(\omega_j)\beta_0\omega_j^0, \quad j = 0, 1, \ldots, S-1. \quad (14)$$

The unknown coefficients α_i ($i = 0, \ldots, N$) and β_i ($i = 1, \ldots, M$) are determined by solving Eq. (14) and setting β_0 to unity. We note that a total of $S \geq M + N + 1$ data samples of the FFT frequency response are necessary to solve Eq. (14).

As mentioned by Dey and Mittra,[23,24] the scaled frequency

$$\omega_s = \frac{2\omega - (\omega_{S-1} - \omega_0)}{\omega_{S-1} + \omega_0} \quad (15)$$

is used in the above procedure to avoid a computational problem due to the very large dynamic range of matrix elements. Here, ω_0 and ω_{S-1} denote the minimum and maximum sampling angular frequencies of ω_j ($j = 0, 1, \ldots, S-1$), respectively.

5. Numerical results

For the Lamé mode resonator shown in Fig. 1, its Lamé mode must satisfy

$$\frac{L_1}{m} = \frac{L_2}{n}, \quad (16)$$

where m and n are integers. Then its resonant frequency f_{exact} is given as

$$f_{exact} = \frac{mV_s}{\sqrt{2}L_1} = \frac{V_s}{\sqrt{2}L}. \quad (17)$$

Here, $V_s = \sqrt{C'_{66}/\rho}$ is the phase velocity of the SV wave, and $L \equiv L_1/m$.[25]

To analyze the resonant frequencies of the Lamé modes, the vibration and observation points are respectively given as $\boldsymbol{p}_v = (3L_1/8 - \Delta/2)\,\hat{x}_1 + (3L_2/8 - \Delta/2)\,\hat{x}_2$ and $\boldsymbol{p}_o = (L_1/8 - \Delta/2)\,\hat{x}_1 + (L_2/8 - \Delta/2)\,\hat{x}_2$. Since the particle velocity components are located at the center of the unit cell of SGCV, $\boldsymbol{p}_v$ and $\boldsymbol{p}_o$ depend on Δ. The x_1-component of the particle velocity, v_1, at $\boldsymbol{p}_v$ is vibrated as a sine-modulated Gaussian pulse with a center frequency of f_{exact} given as $\exp[-\gamma^2(t-t_0)^2]\sin(2\pi f_{exact}t)$, where $\gamma = V_p/(50RL)$ and $t_0 = 150RL/V_p$. After the FD-TD calculation, the FFT or FFT/Padé technique is applied to the time response of v_{x_1} observed at $\boldsymbol{p}_o$ to extract the resonant frequency, f_{FDTD}.

In the following numerical results, the parameters are taken as $R = 0.5$ and $\sigma = 0.25$, where σ denotes Poisson's ratio of the solid.

5.1 Fundamental mode analysis

We consider a square Lamé mode resonator with the side length L [$m = n = 1$]. The time response of v_1 at the observation point in the first 16000 time steps is shown in Fig. 4. Here, $N_l = L/\Delta$ is taken as 2^6.

Figure 5 shows the percentage error in the extracted normalized resonant frequencies, f_{FDTD}/f_{exact}, as a function of N_l. Here, $N_t\Delta_t = 2^{12}RL/V_p = 2^{12}N_l\Delta_t$, where N_t denotes the total number of time steps. The conventional FFT was applied to extract the resonant frequencies. The FD-TD calculations were carried out for whole size, and half and quarter sizes [with the symmetry boundary condition] of the resonator. We can see that these results are identical and that the results converge for $N_l \geq 2^6$. Figure 6 shows the distributions of particle velocity components, v_1 and v_2, at the final time step for $N_l = 2^6$. We can see that the fundamental Lamé mode is excited.

Figure 7 shows the normalized computational time as a function of N_l. Our codes were run on MATLAB in the single-thread mode for more accurate profiling. We can see that computational time can be effectively reduced for larger values of N_l owing to the reduction in the size of the computational domain with the symmetry boundary conditions when we can assume the symmetry of the targeted mode profile. For larger models with $N_l \geq 2^8$, the normalized computational times are slightly smaller than 0.5 and 0.25 for the analyses with half- and quarter-sized computational domains, respectively. The authors think that the reduction in the size of the computational domains is improved cache-hit ratio of the codes.

Figure 8 shows the normalized spectrum of the square Lamé mode resonator as a function of normalized frequency obtained by the conventional FFT and FFT/Padé technique, which are transformed from the same time response by the FD-TD method for $N_l = 2^6$ and $N_t = 2^{14}$. For the conventional FFT, the resonant frequencies are extracted as values on the discretized frequency grid points with the peak values of the frequency response. Here, the number of sampling angular frequencies is taken as $S = N_t/2$ for the FFT/Padé technique. We can see that a finer spectrum and a more accurate resonant frequency are computed by the FFT/Padé technique. Here, the values of M and N in Eq. (12) are taken as eight.

Figure 9 shows the percentage error in normalized resonant frequencies extracted by

the conventional FFT and FFT/Padé technique for the fundamental Lamé mode as a function of the total number of time steps, N_t. We can see that the FFT/Padé technique can easily extract the correct resonant frequencies. The FFT/Padé technique extracts more accurate resonant frequencies than the FFT alone in the range of $N_t \leq 2^{15}$. For $N_t = 2^{11}$, the error in extracted resonant frequency by the FFT/Padé technique is less than 1.2%, but the error by conventional FFT is less than 7.2%. To estimate the resonant frequency with an error less than 0.2%, the FFT/Padé technique and the conventional FFT require 2^{13} and 2^{16} time steps, respectively.

The percentage error in the normalized resonant frequencies extracted by the conventional FFT oscillates for $N_t = 2^{18}$, 2^{19}, and 2^{20} because the fact that the frequency at the peak in the spectrum and the frequency resolution depend on the total number of time steps, N_t, as shown in Fig. 10.

5.2 Higher-order mode analysis

We consider higher-order modes of rectangular Lamé mode resonators with m and/or $n \geq 2$, whose resonant frequencies are given by Eq. (17). In the following numerical results, N_l and N_t are respectively taken as $L/\Delta = 2^6$ and $2^{12}N_l$. The quarter regions of the resonators are calculated by the FD-TD method with the symmetry boundary condition.

Figures 11–13 show the distributions of the particle velocity components for a square resonator with the side length $2L$ [$m = n = 2$] at the 261747th time step, for a rectangular resonator with the length $2L$ and width L [$m = 1$, $n = 2$] at the 261659th time step, and for a rectangular resonator with the length L and width $2L$ [$m = 2$, $n = 1$] at the 261656th time step. We can see that higher-order Lamé modes are excited.

Table III shows the percentage error in normalized resonant frequencies extracted by the FFT/Padé technique and the conventional FFT for the higher-order Lamé modes as a function of the total number of time steps, N_t. Here, $M = N = 8$ and $S = N_t/32$ for the FFT/Padé technique . We can see that the FFT/Padé technique can easily extract the resonant frequencies. The FFT/Padé technique requires $N_t = 2^{10}$ time steps to extract the resonant frequencies with errors less than 2%, but the conventional FFT requires 2^{12} time steps. For $N_t = 2^9$, both methods show deteriorated resonant frequencies. The time period $N_t = 2^9$ corresponds to nearly 1.6 period long of the targeted Lamé mode, and the vibration is insufficient to launch the targeted modes because the number of time steps is very small.

Table I. Parity of elastic field components on a symmetry boundary normal to the x_1-axis. The symbols e and o respectively denote even and odd functions across the boundary.

	Components				
Mode	v_1	v_2	T_1	T_2	T_6
Symmetric	o	e	e	e	o
Antisymmetric	e	o	o	o	e

Table II. Parity of elastic field components on a symmetry boundary normal to the x_2-axis. The symbols e and o respectively denote even and odd functions across the boundary.

	Components				
Mode	v_1	v_2	T_1	T_2	T_6
Symmetric	e	o	e	e	o
Antisymmetric	o	e	o	o	e

However, we observed a field distribution of a non-Lamé mode at larger time steps. For example, Fig. 14(a) shows the distribution of v_1 at the 2^{18}th time step in the same time series as Fig. 13. Figures 14(b) and 14(c) respectively show the distributions of the Lamé mode and residual components separated from the total field by the overlap integral. Figure 15 shows the frequency spectrum obtained by the FFT/Padé technique. We can see that the non-Lamé mode is excited at a frequency of 1.03 MHz. We note that the field distribution shown in Fig. 14(c) and the frequency agree with the results of finite-element analysis. Applying a multi-dimensional Fourier transform may separate the total field into the field of each mode. The non-Lamé components were also observed for the square resonator with the side length $2L$ and for the rectangular resonator with the length $2L$ and width L. We also note that the amplitudes of the non-Lamé components in Figs. 11-13 are very small.

6. Conclusions

For efficient resonant frequency analysis, the symmetry boundary condition and the FFT/Padé technique were applied to the FD-TD method with the SGCV. The proposed method was applied to analyze the resonant frequencies of the fundamental and higher-order modes of Lamé mode resonators on a lossless isotropic solid. The numerical results showed the validity and efficiency of the proposed method. Our future work will address resonant frequency analysis for resonators on solids with loss.

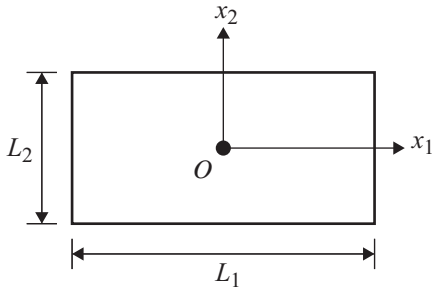

Fig. 1. Two-dimensional rectangular Lamé mode resonator on an isotropic solid with length L_2 and width L_1.

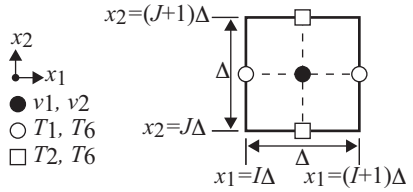

Fig. 2. Unit cell of the staggered grid using the collocated grid points of velocities (SGCV). We note that T_6s represented by the open circles and open squares denote $T_{x_2x_1}$ and $T_{x_1x_2}$, respectively.

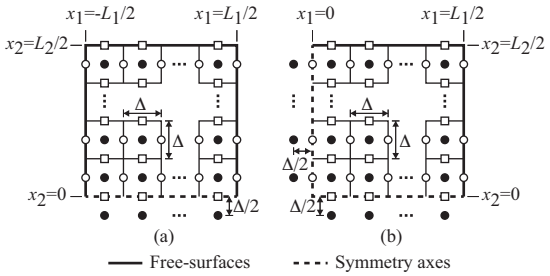

Fig. 3. Lamé mode resonators discretized with the SGCV. The symmetry boundary conditions are imposed on the line, $x_2 = 0$, and the lines, $x_1 = 0$ and $x_2 = 0$, for analysis of (a) half and (b) quarter regions.

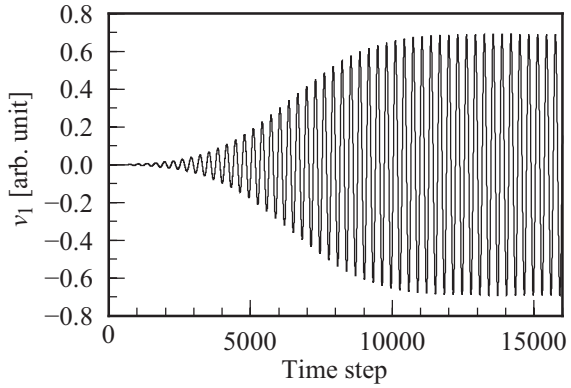

Fig. 4. Time response of a particle velocity component, v_1, at the observation point on the square Lamé mode resonator with side length L in the first 16000 time steps. Here, $N_l = L/\Delta$ is taken as 2^6.

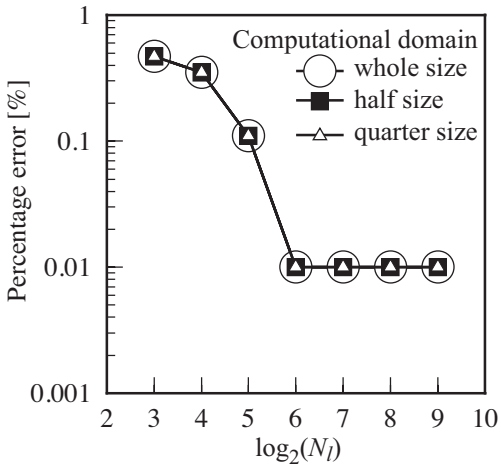

Fig. 5. Percentage error in the resonant frequencies, which are extracted by the FFT, of the fundamental Lamé mode on the square Lamé mode resonator with the side length L as a function of N_l.

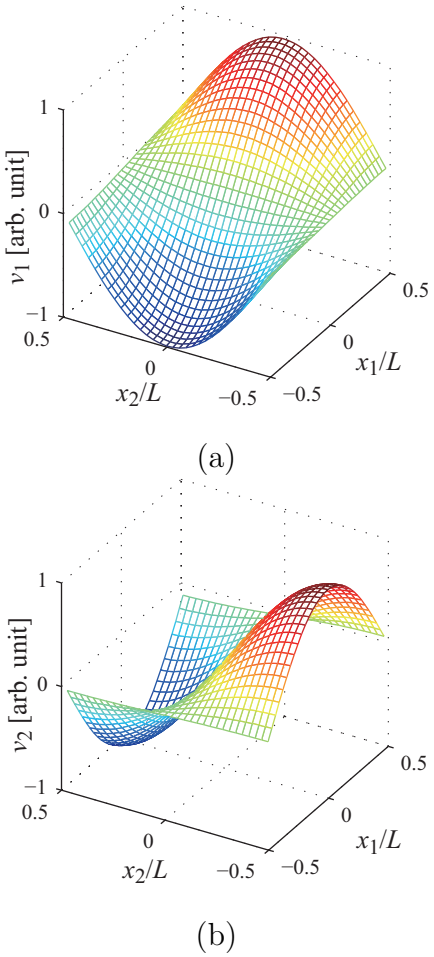

Fig. 6. (Color online) Distribution of the particle velocity components, (a) v_1 and (b) v_2, on the square Lamé mode resonator with the side length L. Here, N_l is taken as 2^6.

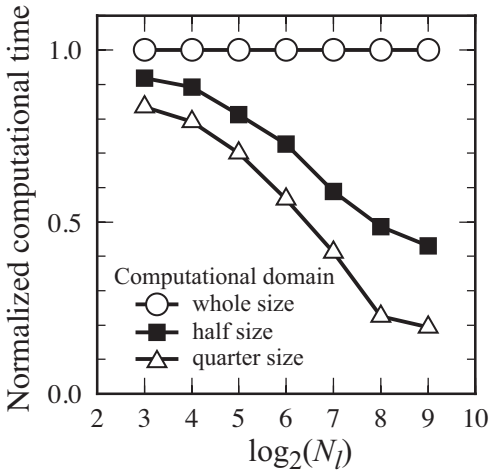

Fig. 7. Normalized computational time as a function of L_l for analyses with whole-, half-, and quarter-sized computational domains.

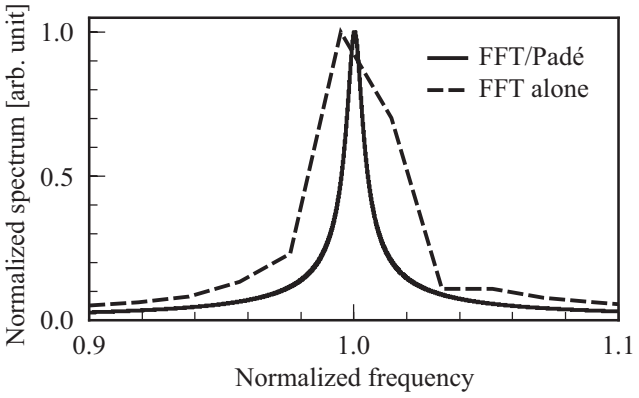

Fig. 8. Frequency spectrum of the square Lamé mode resonator with side length L obtained by the FFT/Padé and FFT methods as a function of the normalized frequency, f_{FDTD}/f_{exact}. Here, $N_l = 2^6$ and $N_t = 2^{14}$ for the FFT and FFT/Padé methodes, and $M = N = 8$ for the FFT/Padé method.

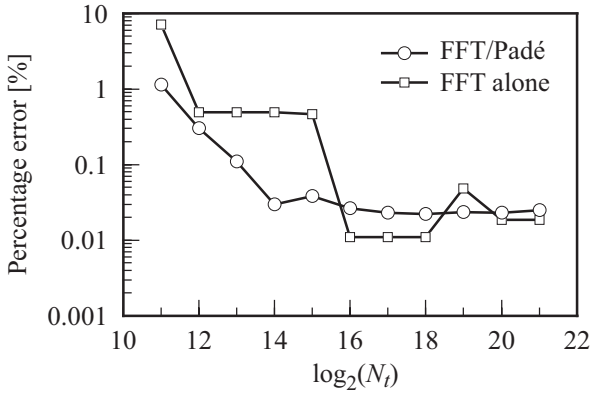

Fig. 9. Percentage error in the resonant frequency of the fundamental Lamé mode obtained by the FFT/Padé and FFT methods as a function of total number of time steps for the square resonator with the side length L. Here, N_l is taken as 2^6.

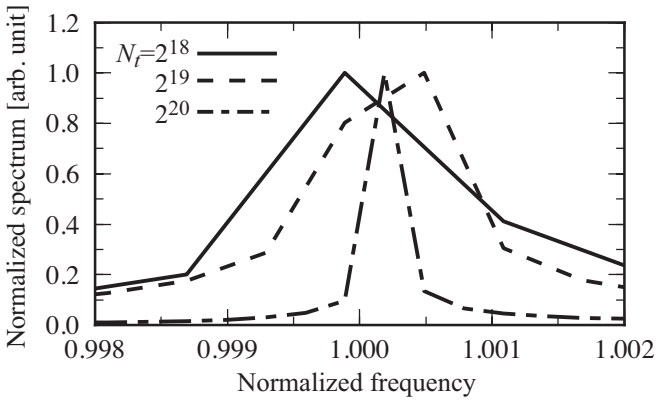

Fig. 10. Spectrum of the square resonator with the side length L as a function of the normalized frequency, f_{FDTD}/f_{exact}, extracted by the conventional FFT for $N_t = 2^{18}$, 2^{19}, and 2^{20}.

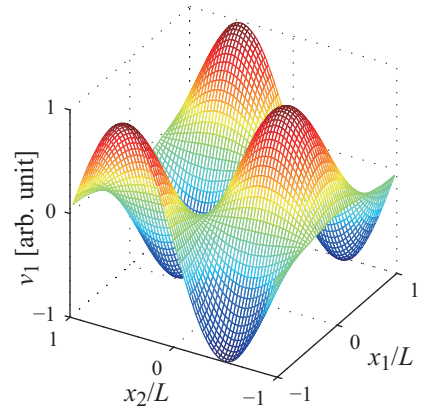

(a)

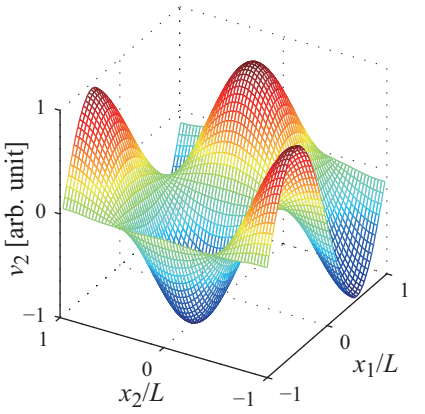

(b)

Fig. 11. (Color online) Distribution of particle velocity components, (a) v_1 and (b) v_2, of a higher-order Lamé mode on the resonator with side length $2L$ [$m = n = 2$] at the 261747th time step.

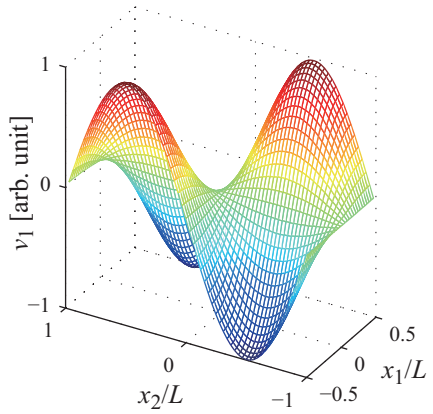

(a)

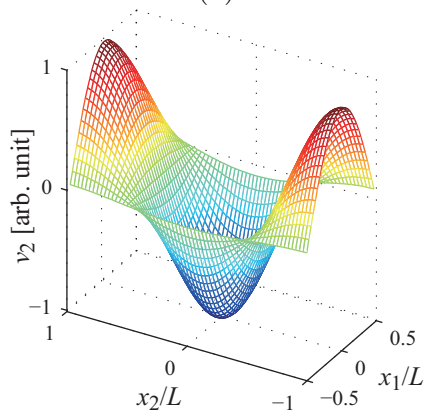

(b)

Fig. 12. (Color online) Distribution of particle velocity components, (a) v_1 and (b) v_2, of a higher-order Lamé mode on the resonator with length $2L$ and width L [$m = 1$, $n = 2$] at the 261659th time step.

Table III. Percentage error (%) in the resonant frequency of higher-order Lamé modes obtained by the FFT/Padé and FFT methods as a function of total number of time steps, N_t.

$\log_2(N_t)$	$m = n = 2$		$m = 1$, $n = 2$		$m = 2$, $n = 1$	
	FFT/Padé	FFT	FFT/Padé	FFT	FFT/Padé	FFT
9	20	39	16	22	20	22
10	0.088	8.1	0.021	8.1	2.0	8.1
11	0.55	8.1	0.46	7.2	0.76	8.1
12	0.22	0.49	0.16	0.49	0.44	0.49
13	0.65	0.49	0.94	0.49	1.3	0.49
14	1.1	0.49	1.6	0.49	0.51	0.49
15	0.54	0.49	0.054	0.47	0.14	0.49
16	0.39	0.011	0.0042	0.011	0.051	0.011
17	0.47	0.011	0.014	0.011	0.013	0.011
18	0.56	0.011	0.020	0.011	0.0070	0.011

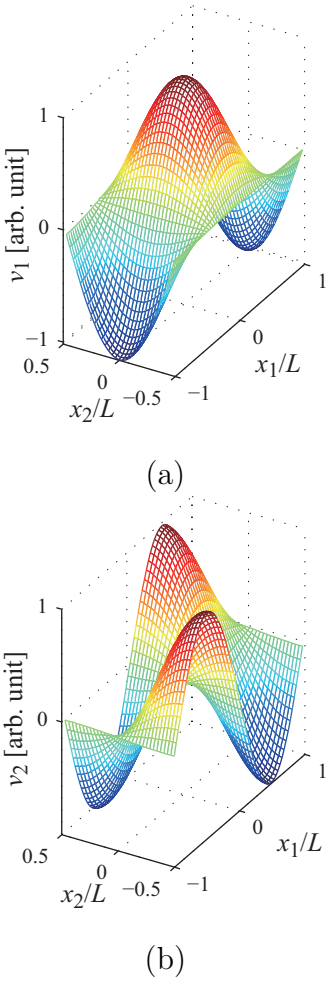

Fig. 13. (Color online) Distribution of particle velocity components, (a) v_1 and (b) v_2, of a higher order Lamé mode on the resonator with length L and width $2L$ [$m = 2$, $n = 1$] at the 261656th time step.

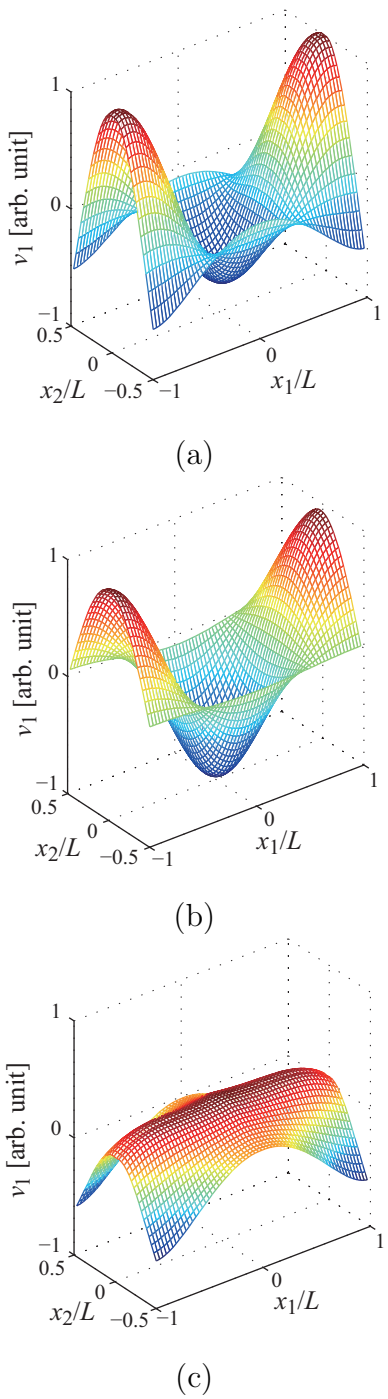

Fig. 14. (Color online) Distribution of a particle velocity component, v_1, of a higher-order Lamé mode on the resonator with length L and width $2L$ at the 2^{18}th time step in the same time series as Fig. 13. Distributions of (a) the total field, (b) the Lamé-mode, and (c) residual components in the total field.

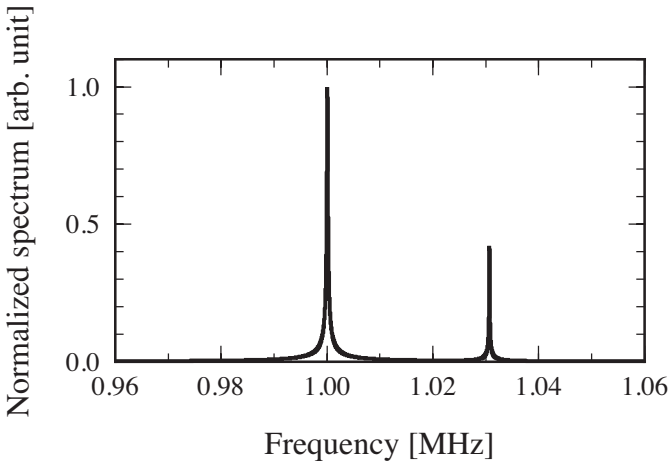

Fig. 15. Frequency spectrum of the rectangular Lamé mode resonator with length L and width $2L$ obtained by the FFT/Padé technique.

References

1) T. Yiyu, Y. Inoguchi, Y. Sato, M. Otani, Y. Iwaya, H. Matsuoka, and T. Tsuchiya, Jpn. J. Appl. Phys. **52**, 07HC03 (2013).
2) K. Kakuma, Y. Norose, K. Mizutani, and N. Wakasuki, Jpn. J. Appl. Phys. **52**, 07HC10 (2013).
3) T. Ishii, T. Tsuchiya, and K. Okubo, Jpn. J. Appl. Phys. **52**, 07HC11 (2013).
4) R. Narumi, K. Matsuki, S. Mitarai, T. Azuma K. Okita, A. Sasaki, K Yoshinaka, S. Takagi, and Y Matsumoto, Jpn. J. Appl. Phys. **52**, 07HF01 (2013).
5) T. Yiyu, Y. Inoguchi, Y. Sato, M. Otani, Y. Iwaya, H. Matsuoka, and T. Tsuchiya, Jpn. J. Appl. Phys. **53**, 07KC14 (2014).
6) S. Maruo and A. Hosokawa, Jpn. J. Appl. Phys. **53**, 07KF06 (2014).
7) S. Tanaka, K. Shimizu, S. Sakuma, T. Tsuchiya, and N. Endoh, Jpn. J. Appl. Phys. **52**, 07HF09 (2013).
8) A. Hosokawa, Jpn. J. Appl. Phys. **53**, 07KF13 (2014).
9) J. Virieux, Geophysics **51**, 889 (1986).
10) A. Levander, Geophysics **53**, 1425 (1988).
11) E. H. Saenger, N. Gold, and S. A. Shapiro, Wave Motion **31**, 77 (2000).
12) T. Bohlen and E. H. Saenger, Geophysics **71**, T109 (2006).
13) M. Sato, Jpn. J. Appl. Phys. **44**, 4490 (2005).
14) M. Sato, Jpn. J. Appl. Phys. **46**, 4514 (2007).
15) M. Sato, Jpn. J. Appl. Phys. **47**, 3931 (2008).
16) V. I. Lebedev, USSR Comput. Math. Math. Phys. **4**, 69 (1964).
17) V. Lisitsa and D. Vishnevskiy, Geophys. Prospect. **58**, 619 (2010).
18) H. Bernth and C. Chapman, Geophysics **76**, WA43 (2011).
19) K. Hasegawa and T. Shimada, Jpn. J. Appl. Phys. **51**, 07GB04 (2012).
20) T. Yasui, K. Hasegawa, and K. Hirayama, Jpn. J. Appl. Phys. **52**, 07HD07 (2013).
21) T. Yasui, K. Hasegawa, and K. Hirayama, Proc. 34th Symp. Ultrasonic Electronics, p. 17, 2013.
22) T. Yasui, K. Hasegawa, and K. Hirayama: Proc. 35th Symp. Ultrasonic Electronics, p. 107, 2014.
23) S. Dey and R. Mittra, IEEE Microwave Guided Wave Lett. **8**, 415 (1998).
24) A. Taflove and S. C. Hagness, *Computational Electrodynamics: The Finite-Difference Time-Domain Method* (Artech House, Norwood, MA, 2005) 3rd

ed., p. 694.

25) R. D. Mindlin, J. Appl. Phys. **27**, 1462 (1956).